



# UHPC girder multi-modal deformation measurements: Photogrammetry, physical sensing, and FEA

Georgios Apostolakis, Kevin R. Mackie, Mostafa Iraniparast, Peng “Patrick” Sun \*

Department of Civil, Environmental, and Construction Engineering, University of Central Florida, 12800 Pegasus Drive, Orlando, FL 32816, USA

## ARTICLE INFO

### Keywords:

Bond strength  
Photogrammetry  
3D digital image correlation  
Finite element analysis  
Flexural failure  
Normal-strength steel  
Ultra-high performance concrete

## ABSTRACT

Ultra-high performance concrete (UHPC) has become increasingly popular in flexural design of structural members that require high performance. Although numerous experimental studies on passively reinforced UHPC flexural members exist, studies on monolithic members with larger cross sections are limited, and no information exists on full-field deformation measurements of such specimens. An experimental program consisting of 8 large-scale UHPC doubly-reinforced specimens with continuous longitudinal rebars was conducted under 4-point monotonic loading. The experimental objectives were to investigate rebar slip from one side of the specimens (longitudinal rebar with hooks only on one side), track crack propagation, and capture the full-field displacement and strain measurements during the loading. The noncontact measurements from the multi-camera computer vision system using 3D digital image correlation (3D-DIC) and AprilTag-based photogrammetry were compared with the physical (contact) displacement measurement system. Strain fields were obtained using dual-camera 3D-DIC and finite element (FE) analysis. Results showed a close agreement of the point-wise displacements obtained from the physical and computer vision monitoring systems. The asymmetric structural design caused slip that delayed rebar fracture and reduced the peak load below that predicted by sectional analysis. The measured global force-deflection curve was predicted by the FE model when using a calibrated bond-slip model between rebar and UHPC. Comparison between the full-field measurements using 3D-DIC and FE numerical models showed that the evolution of principal strains and cracking were consistent. 3D-DIC proved to be a promising measurement method for monitoring strain/displacement and calibrating/confirming FE model that conventional methods without full-field measurements cannot provide.

## 1. Introduction

Ultra-high performance concrete (UHPC) is a high strength cementitious composite material with fiber reinforcement that has seen rapid deployment in recent structural engineering research and practice. The acceleration in UHPC research was significantly promoted after commercial and non-proprietary mixes became available [17]. UHPC-class materials are characterized by enhanced durability and mechanical properties far exceeding those of conventional normal-strength and high-strength concrete. The increased compressive, tensile, and bond strengths enable sections with greater capacity and reduced size than traditional reinforced concrete. However, due to the increased unit cost, utilization of UHPC has often been confined to cast-in-place joints or low-profile systems that minimize concrete volume. Only in the last ten years have there been multiple flexural studies on medium- and large-scale monolithic UHPC sections and contributions to predicting

flexural strength [11,29], shear strength [18,1], and design specifications (e.g., AASHTO guide specification as described in [13]).

While component- and material-level tests have been conducted to calibrate UHPC constitutive, sectional, flexural, and continuum models, they are limited by the drawbacks of standard physical measurement systems. Particularly, load-dependent profiles or maps of displacement, curvature, or strain are limited by the number and position of devices. Although there are non-contact sensing systems to measure displacement [e.g., laser-based displacement sensors [46], LiDAR [20]] and strain [e.g., laser-induced strain sensor using Raman spectroscopy [31] and near infrared (NIR) photoluminescence spectroscopy [22,36,37] on nano materials], full-field measurements with acceptable accuracy and low cost are needed for larger infrastructure members. Promising methods include affordable photogrammetric methods, such as digital image correlation (DIC) [23,4] and machine vision [8].

The mechanical properties of UHPC, e.g., compressive strength >

\* Corresponding author.

E-mail address: [peng.sun@ucf.edu](mailto:peng.sun@ucf.edu) (P.P. Sun).

<https://doi.org/10.1016/j.istruc.2024.107790>

Received 30 April 2024; Received in revised form 8 October 2024; Accepted 6 November 2024

2352-0124/© 2024 Institution of Structural Engineers. Published by Elsevier Ltd. All rights are reserved, including those for text and data mining, AI training, and similar technologies.

150 MPa and a post-cracking tensile strength  $> 5.0$  MPa [12], are affected by many factors including curing type (thermal, steam, ambient, etc.), curing time, and steel micro-fiber reinforcement. High strength steel micro-fiber reinforcement (volume fractions  $\leq 5\%$ ) facilitates tension hardening, higher tensile ductility, increased post-peak energy dissipation capacity, spalling resistance, and enhanced bond strength [12]. UHPC offers improved bond strength and confinement behavior over conventional reinforced concrete (RC), reducing development length and confinement steel requirements.

Medium- and large-scale flexural studies on UHPC members (sections with minimum 200 mm depth) have proliferated since availability of premix materials (both commercial and non-proprietary), fibers, and mixing/placement methods allowed larger monolithic members rather than only for connections and repair. Numerous tests have been conducted on rectangular sections with passive tension reinforcement and with or without transverse reinforcement. Of those studies, it was found that fiber volume fractions of 1.5–3% were typically needed to develop the post-cracking tension hardening behavior that is typical with UHPC [10,32,47]. Studies with various longitudinal reinforcement ratios found that 1.5% to 3% resulted in more ductile responses [10,30,40,45, 47]. From the studies where specimens exhibited stable peak strength, it was observed that all of them contained compressive reinforcement. However, the predominant response observed amongst beam tests was post-peak softening [34,43,44]. As long as the shear span to depth ratio was limited to 2 or larger, flexural cracking patterns were observed with the failure defined by a single large crack opening underneath one or both load points rather than flexural-shear or shear failure.

DIC [39] is a non-contact method for monitoring material deformation using image registration methods to firstly ascertain the relative displacements of feature points between a reference (undeformed) image and a current (deformed) image. Due to its high-resolution and non-invasive capabilities, DIC is an invaluable tool for assessing and maintaining infrastructure [41]. Earlier researchers used two-dimensional (2D) DIC to study strain distribution [5], cracking development [19], and flexural behavior [7] of concrete beams as well as the strain and crack distributions of confined masonry walls [14]. Although 2D displacement measurement in 2D-DIC or 2D-photogrammetry is relatively straightforward, it proves inadequate in capturing the out-of-plane displacement [28]. Unlike 2D-DIC, which is prone to errors from even minor out-of-plane displacements, 3D-DIC (or stereo-DIC) utilizes two synchronized cameras to provide enhanced accuracy by measuring three displacement components simultaneously [2]. Full-field object contour, displacement, and strain distributions can be measured simultaneously by 3D-DIC under different loading conditions. Therefore, in recent years, 3D-DIC methods have been employed in the experimental studies of concrete structures, such as normal concrete beams [21], seawater sea-sand coral concrete beams (Yuan et al., 2021) and FRP confined concrete specimens [48].

Experimental studies of UHPC members using DIC methods are mainly within a narrow spectrum at small scales. For example, material-level and component-level tests of UHPC members include studies of tensile behavior using dumbbell-shape coupon specimens [33], flexural behavior and fracture patterns using small beams (width  $\leq 100$  mm, depth  $\leq 100$  mm, length  $\leq 400$  mm) [24,27], freezing and thawing behavior using coupons and small beams [41], bending-tensile behavior using small concrete prisms [15], and fatigue crack development using cyclic loading on small beams [26]. Although there are a few experimental studies on medium or large-scale components (span  $> 1000$  mm, scale  $\sim 0.6$ – $0.7$ ), the studies used small cross-section, big-size patterns [e.g., grid pattern [38], circular tags [6]] providing coarse spatial resolution in strain measurements, and/or commercial 2D-DIC software product [32].

The objective of this study is to investigate the flexural and shear responses of large-scale continuously reinforced UHPC girders using multi-modal sensing systems (fiducial marker-based vision and 3D-DIC). Eight flexural UHPC specimens were tested to failure under four-point

loading. The girder specimens had nominally identical sections (depth of 254 mm and shear span-to-depth ratio of 2), normal-strength longitudinal reinforcement, and no transverse reinforcement. Due to concrete, rebar bond, and fiber size effects, it is important to study components at full-scale or near-full-scale, and to the authors' knowledge, there have been no previous noncontact monitoring studies of UHPC flexural specimens at this scale. In addition, there is lack of study on the bond-slip mechanism at high loads in UHPC specimens, which can be enabled by a different reinforcement detail with longitudinal bars hooked at one end and straight at the other.

The evolution of displacement, strain, and cracks with load were obtained using a novel multi-camera computer vision system consisting of multiple industrial cameras, customized synchronization algorithm, fused patterns of paint-based speckles and paper-based AprilTag's [42]. Experimental load-displacement responses were compared between sensing systems and the results demonstrate how the fused computer vision results render the traditional physical measurement redundant. Full-field displacement and strain measurements from computer vision were compared with the results from calibrated sectional and continuum finite element (FE) models to demonstrate extension beyond single-point measurements.

## 2. Experimental program

### 2.1. Materials

The commercially available UHPC product Cor-Tuf CT25 was used, with a target compressive strength of 172 MPa under controlled curing conditions. Cor-Tuf CT25 is composed of proprietary pre-blended constituents, local masonry sand, Portland cement, water, high range water reducing admixture, corrosion inhibitor, and 2% smooth straight steel fiber content by volume. The fibers are 0.203 mm in diameter and 12.7 mm in length. A comprehensive set of material tests conducted to characterize the UHPC material properties are summarized in Table 1.

### 2.2. Girder Specimens

The experimental program consisted of eight large-scale UHPC beam flexural tests. The cross-section dimensions were 254 mm in depth, 279.4 mm in width, and the lengths of span were either 1066.8 mm or 1117.6 mm. The spacing between the two load points was 76.2 mm. The testing matrix consisted of beams denoted G1N, G1S, G2N, G2S, G3N, and G4N with 1117.6 mm clear span, and G5N and G5S with 1066.8 mm clear span. A schematic of the cross section and flexural setup are shown in Fig. 1.

Both tension and compression US #8 longitudinal bars with diameter  $d_b = 25.4$  mm were installed. All reinforcement was ASTM A615 grade 60 mild steel with 90-degree hooks at the left support and straight bars extending beyond the specimen face on the right support (to investigate possible slip from one side under large flexural loads). The clear cover of

**Table 1**  
UHPC (Cor-Tuf CT25) material properties characterization tests. Hock et al., [16].

Test	Age (day)	Result at time of test
Uniaxial Cylinder Compression Test (ASTM C1856)	28	Strength 172 Mpa (25 ksi)
Third-point Loading Flexure Test (ASTM C1609) 4 × 4 × 14in (101.6 × 101.6 × 355.6mm)	29	Peak load: 70.2 kN (15.8 kip) Deflection: 0.457 mm (0.018 in)
Split Cylinder Tensile Test (ASTM C496)	28	Strength: 17.2 MPa (2.5 ksi)
Modulus of Elasticity / Poisson' Ratio Test (ASTM C469)	28	Modulus: 49,815 MPa (7,225 ksi) Poisson's ratio: 0.19

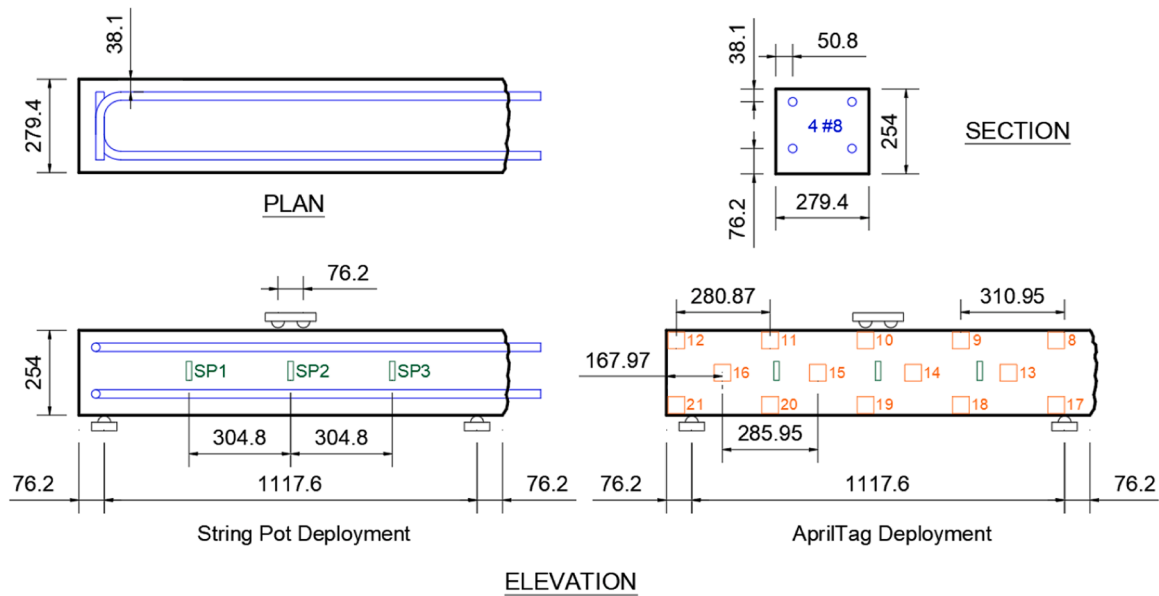


Fig. 1. Schematic of experimental setup of UHPC flexural girder specimen (unit: mm).

the reinforcing bars to the tension and compression face of the specimens was  $C_s = 1.0d_b$ , and  $C_s = 2.5d_b$ , respectively. The longitudinal steel reinforcement ratio ( $A_s / A_c$  or  $A_s' / A_c$ ) was 1.4 % for both the tension and compression steel ( $A_s = A_s'$ ). No transverse shear reinforcement was required in any of the specimens due to the high tensile and shear strength of UHPC.

The fabrication of the girders was performed in the Structures Laboratory at the University of Central Florida. All specimens were cast in plywood formwork, which was initially painted with interior latex-based paint and then coated with mineral oil before casting to facilitate removal. Each specimen was cast (using a ready-mix truck with standard chute) from the center to ensure an even fiber dispersion and flow alignment at the midspan. All specimens were wetted with a proprietary solution and ambient cured for 70 days prior to testing.

### 2.3. Testing methods and sensing systems

#### (a) Loading Protocol

The girders were tested under displacement control at a rate of 12.7 mm/min using a servo-controlled MTS actuator with 490 kN capacity and a Newton controller. The actuator was connected vertically to a self-reacting steel frame, and the girder half-round steel spherical bearings were seated upon concrete buttresses. The testing protocol was terminated when the load was reduced to approximately 20 % of the peak load capacity with a sudden drop. The loading protocol included steps of monotonic increments at 0.25 % drift (2.8 mm) up to 4 % drift level (44.7 mm), followed by increments at 0.5 % drift (5.6 mm) until the specimens failed, typically following the fracture of the tensile reinforcing bars. The testing was paused between every increment to closely inspect the specimens and mark/photo document crack development and progression.

The physical measurement system consisted of two support linear variable displacement transducers (LVDTs) that were mounted on each specimen's ends to capture support displacement effects, and three displacement string pots mounted at the midspan and 304.8 mm from the midspan of each side to measure the deflection profile of the girders. The LVDTs at the supports were Sensata-BEI 38.1 mm LVDTs, and string pots at the midspans were Micro-Epsilon (wire wound potentiometric sensors 1250 mm WPS-1250-MK46-CR-P10). The displacements and

Newton controller load were acquired using a data acquisition system (National Instruments) with a recording frequency of 10 Hz.

#### (b) Camera System and Patterns

A multi-perspective vision system was set up consisting of eight industrial-grade machine-vision cameras (MV-CA050-10GM, Hikrobot, China) with manually interchangeable lens of 4 - 12 mm. Four of the cameras were positioned along each of one face of the specimen and used as pairs of dual-perspective systems to obtain the 3D displacements. The parameters of all the cameras were set as the same, e.g., focal length = 4 mm and frame rate = 2 frame per second (fps). All the cameras were placed around the specimens and were connected by ethernet cables (RJ45 Cat 6e) through a Gigabit ethernet network switch to a Linux-based computer. The data collection on the cameras was synchronized using a python-based custom controlling software with the core functions in C programming.

Thirty-six "family 36h11" AprilTags with dimensions of 40 mm × 40 mm (pattern size) on 50 mm × 50 mm sticky papers (with white margin) were used as the visual markers on one side of the specimens (Fig. 2). The ground-truth locations of the AprilTags were measured using tape measurement, assuming the three edges of the concrete girders at corners are straight and orthogonal to each other. The origin of the global world coordinate system (WCS) was set at the corner of the girder with the x-axis oriented along the axial direction, the y-axis along the depth, and the z-axis along the vertical direction of the girder. The global WCS was fixed regardless the deformation of the girders. A randomly distributed (in local) speckle pattern was applied on a roller-brush with a proper density of 8-12 ct./cm<sup>2</sup> so that the sizes of the speckles ranged between 1 mm and 4 mm for a relatively fine-resolution DIC strain measurement.

#### (c) Camera Calibration and Image Collection

Both 3D-DIC and AprilTag detection algorithms required camera calibration in which checkerboards were adopted for the intrinsic calibration, and the mounted AprilTags were used for the extrinsic calibration. The intrinsic parameters of a camera consist of the essential characteristics that are inherent to that individual camera, including the focal length, principal point, and lens distortion coefficients. The extrinsic parameters include the camera locations and poses which can be used to determine

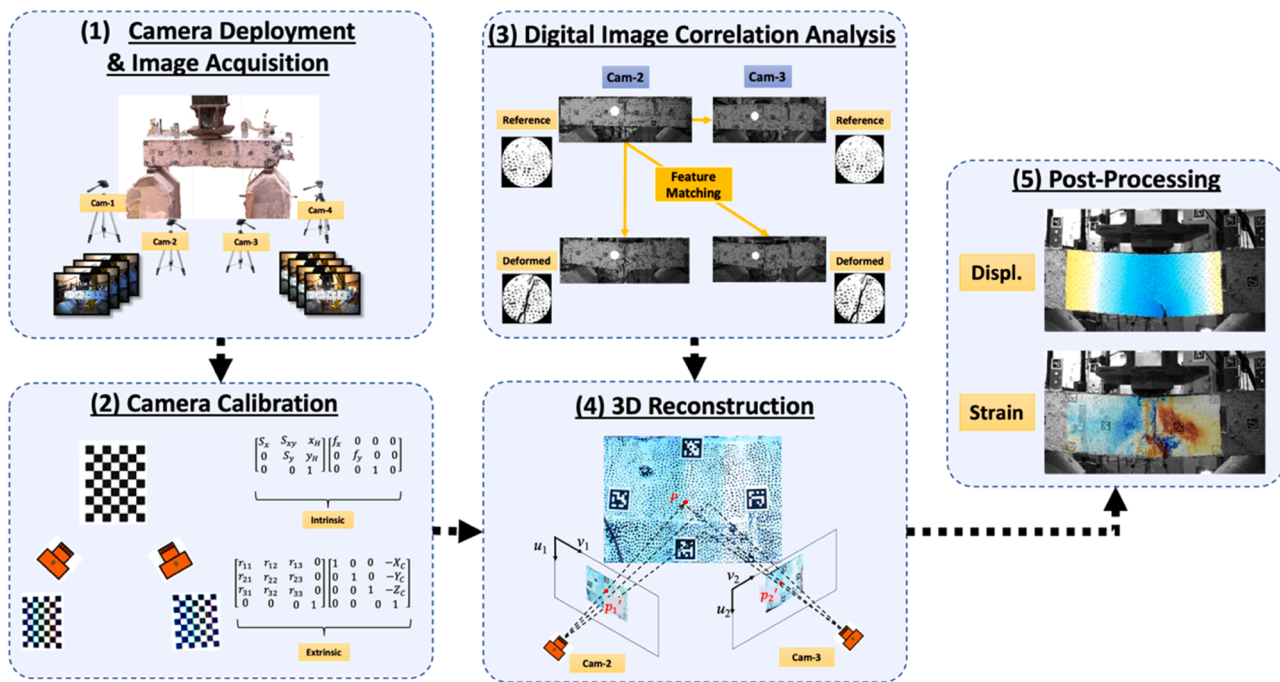


Fig. 2. Schematic view of 3D-DIC method with steps.

the spatial orientation of the cameras with respect to the experimental scene. Because the real-time acquisition of images is essential to precisely examine the behavior of UHPC beams when subjected to external loads, a camera system configuration was used during the experiments to consistently collect images in real time (e.g., 2 fps).

### 3. 3D-DIC method and strain mapping

Feature matching in 3D-DIC was accomplished by setting up the region of interest (ROI) from both the reference and current image frame  $f_i$  at time  $t_i$ . The ROI on the UHPC beams (e.g., in the middle part, as shown in Fig. 2) used speckle patterns to compute displacement and strain. Once the ROI was determined on the first image, appropriate DIC parameters (subset radius, subset spacing, etc.) were selected to accurately correlate the speckle patterns across image sets, e.g., each subset should be large enough to contain at least 2–3 speckles (Sutton 2009). Normalized cross-correlation technique was used in the NCORR software [3] to detect and map related points between the reference and deformed images. The mapping entails constructing a mesh of triangular elements over the ROI, which is required for subsequent 3D reconstruction and strain computation.

Due to the long duration of image collection (1.5–2.5 hrs), streamlined data processing of 3D reconstruction was conducted using the obtained calibration parameters to convert the correlated features obtained from 2D image plane into 3D triangular meshes in the WCS. The transformation was accomplished by using stereo triangulation methods, such as direct linear transform (DLT). The 3D coordinates of the matched features were used to compute displacement fields. Every triangular mesh element employed the Cosserat point element procedure [25] to compute the strain fields.

The first frames from the cameras were chosen as the reference images for 3D-DIC processing. The study adapted an open-source Matlab software, DuoDIC [35], as the backbone for 3D-DIC analysis with a feature matching function using NCORR software [3] to effectively localize the matched features in 3D WCS from stereo image pairs. The stereo-camera calibration module (using Matlab toolbox) within the 3D-DIC backbone was replaced by a custom individual camera

calibration to better address the unique requirements in the experiment. The unique requirements included the accommodations for multiple tests with different camera deployment around each specimen and for the difficulty in using the narrowed space between camera and specimens ( $\sim 1$  m) for (intrinsic) calibration. Fig. 2 shows the five steps included in the 3D-DIC of this study: (1) image acquisition; (2) individual (intrinsic) camera calibration using checkerboards; (3) feature matching using images of deformed structure to the reference image; (4) 3D reconstruction using DLT processing and triangle meshing; and (5) post-processing for strain mapping and visualization.

Principal strains ( $\epsilon_{p1}$  and  $\epsilon_{p2}$ ) and orientations of principal strains ( $\theta_{p1}$  and  $\theta_{p2}$ ) were computed based on the eigenvalues and eigenvectors of the general Cauchy strain matrix ( $E$ ):

$$E = \begin{bmatrix} \epsilon_{xx} & \epsilon_{xy} \\ \epsilon_{xy} & \epsilon_{yy} \end{bmatrix} \quad (1)$$

where  $\epsilon_{p1}$  and  $\epsilon_{p2}$  correspond to the maximum and minimum eigenvalue, respectively. The same procedure was applied for principal strain and angle calculation to both the 3D-DIC and numerical model results.

### 4. Numerical modeling

To further investigate the full-field displacement and strain measurements obtained using computer vision, a continuum plane stress FE model was developed and calibrated in OpenSees. The plane stress model utilized isoparametric quadrilateral elements for the UHPC material, displacement-based nonlinear beam elements for the rebar, and nonlinear springs for the interfacial bond between UHPC and rebar. In addition, section equilibrium analysis was conducted to compare the strength estimates obtained from the experimental and continuum model results.

#### 4.1. Numerical model geometry

The general geometry layout used to model each beam specimen within OpenSees is illustrated in Fig. 3. This layout has six main components: inelastic quadrilateral elements between the centerline of the supports, elastic quadrilateral elements that represent the extension of

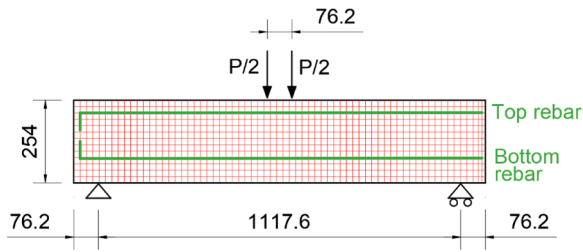


Fig. 3. Finite element mesh used for plane stress continuum analysis.

the specimen beyond the supports (with one side longer than the other where the longitudinal bars were hooked), a beam with steel circular fiber section for each of the top and bottom continuous rebars, a bond-slip (horizontal) spring with zero length connected to rebar, and a dowel action (vertical) spring with zero length connected to rebar. The explicit rebar beam elements were modeled as single beam elements top and bottom (with sections containing two rebars) and located at the correct geometry relative to the UHPC section dimensions (therefore, the spring elements may have finite lengths depending on the mesh discretization for the concrete).

The horizontal discretization of the model was calibrated to ensure a constant aspect ratio and minimum element size of 19.1 mm. The presented results utilized a uniform discretization of 56 elements in the longitudinal direction (between supports) and 13 elements in the vertical direction. Due to the stiffness of the specimens and the small-span lengths, only small displacements were considered in the model. Two-point loads were applied to the concrete beam at the same locations as the experimental specimen, and the boundary conditions were pinned at the left end of the concrete beam and roller at the right end of the concrete beam.

#### 4.2. Constitutive models

Each component of the model has a specific constitutive model associated with it to capture all nonlinear effects of the flexural specimens. The *LowTension* plane stress constitutive model was selected to represent UHPC. Before cracking, the material exhibits isotropic elastic behavior. Cracking (fixed cracking angle) is determined using the principal tensile stress. After cracking, the material exhibits orthotropic behavior. The tension backbone has tension hardening followed by tension softening (piecewise linear). The compression backbone follows

that of the *Concrete02* uniaxial constitutive model, as do the unloading/reloading rules. The principal stress-strain curve (Fig. 4b) used in the analysis as well as the corresponding parameters are shown in Table 2.

The steel reinforcing constitutive model was a modified version of *Steel02*. It contained an ultimate stress and strain, after which the backbone softens linearly to fracture (total loss of resistance). The parameters of the model were  $F_y = 448$  MPa,  $F_u = 717$  MPa,  $E = 200,000$  MPa, strain at ultimate stress 0.107, rupture strain 0.14,  $R_0 = 18$ ,  $c_{R1} = 0.925$ , and  $c_{R2} = 0.15$ . The reinforcing steel interacts with the surrounding concrete through two mechanisms: bond-slip (tangent to bar) and dowel action (normal to bar).

The bond stress-slip mechanism is represented by the *MultiLinear* material model, having slip and stress inputs. The shape of the bond-slip curve was adopted from the original form proposed by [9] for normal strength concrete; the general bond force-slip material model is shown in Fig. 4a. The slip inputs  $u_1$  to  $u_3$  and bond inputs  $f_{peak}$  and  $f_{res}$  were the values calibrated from inverse analysis in previous studies on small-scale UHPC beams [16] utilizing the same UHPC material as the present study. The stress inputs were converted to force units for the *zeroLength* spring elements using the tributary length of rebar and the rebar perimeter. Unlike the infinite plateau residual stress  $f_{res}$  in most models,  $u_4$  and  $f_4$  were assumed to be 5.1 mm and 0.7 MPa, respectively. The bond strengths were multiplied by 0.75 since there were only continuous bars in the present study (not lapped as in [16]). It should be noted that other UHPC beam modeling studies have assumed perfect bond with no slip allowed [32,34,45].

Dowel action is the ability of reinforcing bars to carry shear force due to slipping of cracked surfaces normal to the reinforcing bar. This is used

Table 2  
OpenSees UHPC material properties.

Parameter	Symbol	Value
Uniaxial Compressive Strength, MPa (ksi)	$f_c$	152 (22)
Youngs Modulus, MPa (ksi)	$E_c$	48263 (7000)
Tensile Strength, MPa (ksi)	$f_t$	6.2 (0.90)
Ultimate Tensile Strength, MPa (ksi)	$f_{tu}$	7.6 (1.10)
Ultimate Tensile Strain	$e_u$	0.0035
Residual Tensile Strength, MPa (ksi)	$f_{res}$	0.9 (0.13)
Residual Tensile Strain	$e_{res}$	0.025
Maximum Strain	$e_{max}$	0.035
Ultimate Strain Multiplier	$c_{max}$	2.0
Ultimate Strain Multiplier	$t_{max}$	1.0

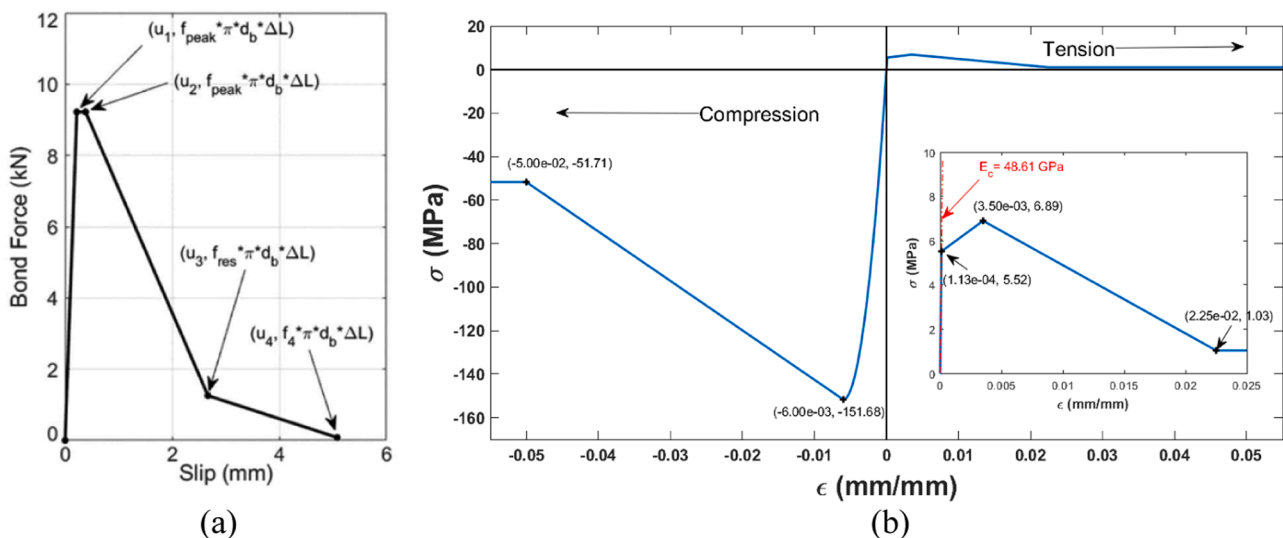


Fig. 4. (a) Bond force-slip backbone curve of rebar-UHPC interaction, and (b) stress-strain curve of UHPC material in OpenSees FE simulation (with inset showing tension part).

**Table 3**  
OpenSees reinforcing material properties.

Parameter	Symbol	Value
Yield Stress in Tension, MPa (ksi)	$f_y$	448 (65)
Ult. Stress in Tension, MPa (ksi)	$f_u$	717 (104)
Initial Elastic Tangent, MPa (ksi)	$E_s$	199948 (29000)
Tangent at Initial Strain Hardening, MPa (ksi)	$E_{sh}$	8998 (1305)
Strain at Initial Strain Hardening	$e_{sh}$	0.0070
Strain at Peak Stress	$e_{ult}$	0.1170

to define the perpendicular interaction between the rebar and the surrounding concrete. Due to the large cover distance to the tension face of the girders, the dowel action mechanism was represented by uniaxial elastic model. The normalized (by the bottom cover distance) stiffness was the same as that used in Hock et al. [16].

#### 4.3. Analysis and outputs

The analysis used displacement control based on the midspan vertical deflection and automatically adjusted the step size to ensure convergence up to a displacement target of 63.5 mm. Results from the quadrilateral elements were extracted for post-processing and compared with the DIC measurements at discrete displacements of 6.35, 12.70, 19.05, 25.40, 31.75, 38.10, and 63.50 mm. The strain field ( $\epsilon_{xx}$ ,  $\epsilon_{yy}$ ,  $\epsilon_{xy}$ ) at each integration point was extracted from the FE results, along with the principal strains, current principal angles, and strains relative to the crack obtained from Mohr's circle and transformation matrix were obtained at each integration point (specific to the *LowTension* material).

#### 4.4. Sectional analysis

The same tension backbone and parameters defining the backbone were used as the response in the principal direction of the plane stress model (however now in only the normal stress direction due to sectional analysis). The compressive behavior of UHPC was assumed to be piecewise linear with the same  $f_c$  as the numerical model. The plateau at  $f_c$  extended to a strain of  $-0.004$  before a linear softening branch to the same ultimate strain used in the *LowTension* model. The steel reinforcing bar section, constitutive model, and parameters defining the backbone were the same as those used in the plane stress model.

Moment-curvature analysis was performed by imposing monotonically increasing curvature values on the section under constant axial load (zero axial). The applied loads (from the four-point bending configuration) that correspond to the nominal moment and the ultimate capacity were 445 kN and 503 kN, respectively. For comparison, the shear capacity of the section computed according to the AASHTO guide specification is 587 kN. The section behaviors were then integrated along the length of four displacement-based beam elements representing the geometry, boundary conditions, and point loads of the experiment.

Load-displacement analysis was conducted using the one-dimensional elements under a monotonically increasing mid-span displacement.

## 5. Experimental results

The experimental results for the girders are presented in terms of the force-deflection history and deflection time-history at the three locations of the physical sensors. Measurements obtained by means of physical sensors were compared against the results obtained by AprilTag and DIC image processing at the same locations.

### 5.1. Force-deflection comparison

Applied load versus midspan deflection histories for all girder specimens are shown in Fig. 5. The force was recorded from the hydraulic actuator channel, while the midspan deflections of the girders were measured using three modalities: string pots (SP), AprilTag, and 3D-DIC. Midspan deflection measurements include all the eight girder specimens using string pots and AprilTag, and four processed measurements for girders G1S/G2S/G3N/G5S using 3D-DIC. The force-deflection plots created using the three selected displacement measurement modalities were very close over the range. To further assess any differences between the three displacement measurement modalities, the force-deflection responses at the midspans are shown in Fig. 6 and Fig. 7. It is seen that the force-deflection plots among SPs, AprilTags, and DIC measurements were almost identical for the full range of the plots.

Exceptions in agreement across modalities include the horizontal path of SP deflection for girders G2N and G5N. The discrepancies happened because a crack that developed in the midspan of the girders crossed the bracket attaching the SP wire. The bracket was ultimately detached from on the girder surface due to the crack. For G2N the full plot was recorded since the SP bracket was detached at the end of the test only when the tensile reinforcing bar fractured. However, for G5N the discrepancy happened earlier at the peak of the force-deflection plot. Nonetheless, the experimental measurements were still recovered by using the measurements from the AprilTag and/or 3D-DIC. For G5S there was an erroneous reversal of deflection at the transition from elastic to inelastic response in the SP measurement, in this case possibly due to issues with the voltage or the wire connections since later in the test the SP measurement trend followed the AprilTag and DIC measurements with a finite offset (hereby the physical measurement verified using the measurements from the AprilTag and DIC). Lastly for G4N (Fig. 6b), while the AprilTag measurement followed the SP measurement closely, drift occurred after the peak load.

### 5.2. Deflection comparison

To better understand the above behaviors, the midspan deflection time-histories are plotted in Fig. 8 and Fig. 9 for each girder to compare

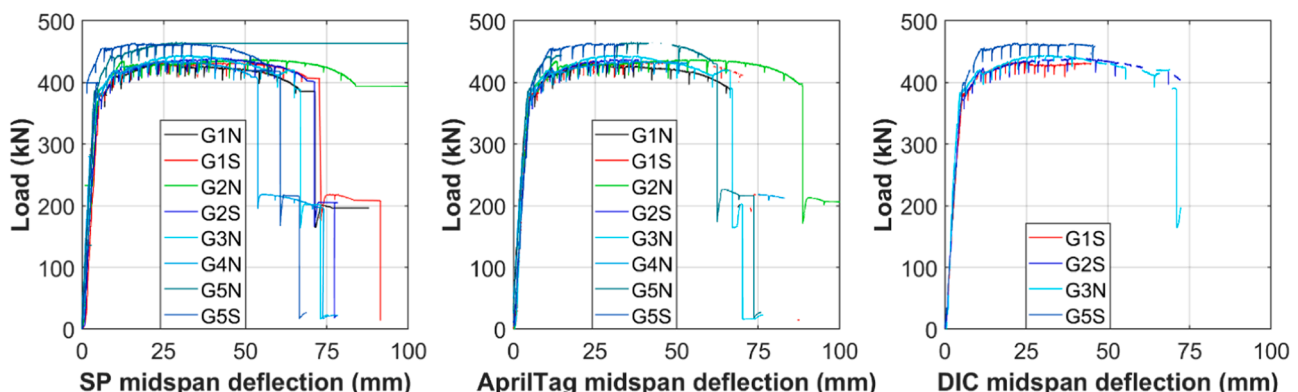


Fig. 5. Girder experimental force versus deflection at the mid-span measured with string pots (SP), AprilTag, and DIC methods.

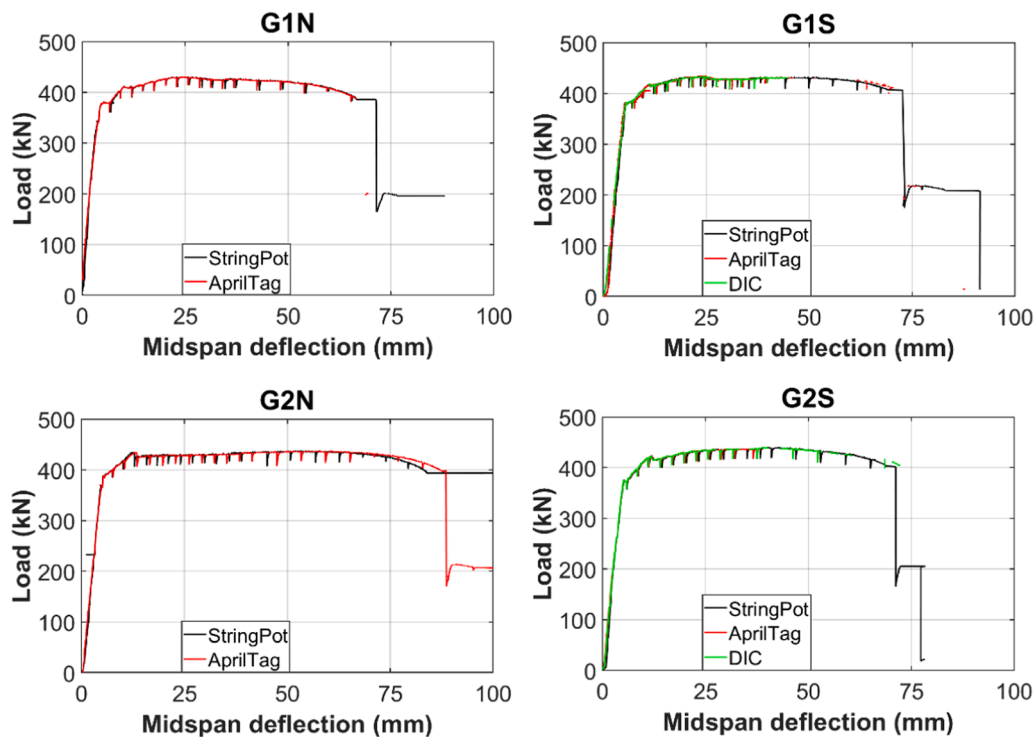


Fig. 6. Girder G1N/G1S/G2N/G2S experimental force versus deflection at the mid-span measured with String Pots (SP), AprilTag, and DIC methods.

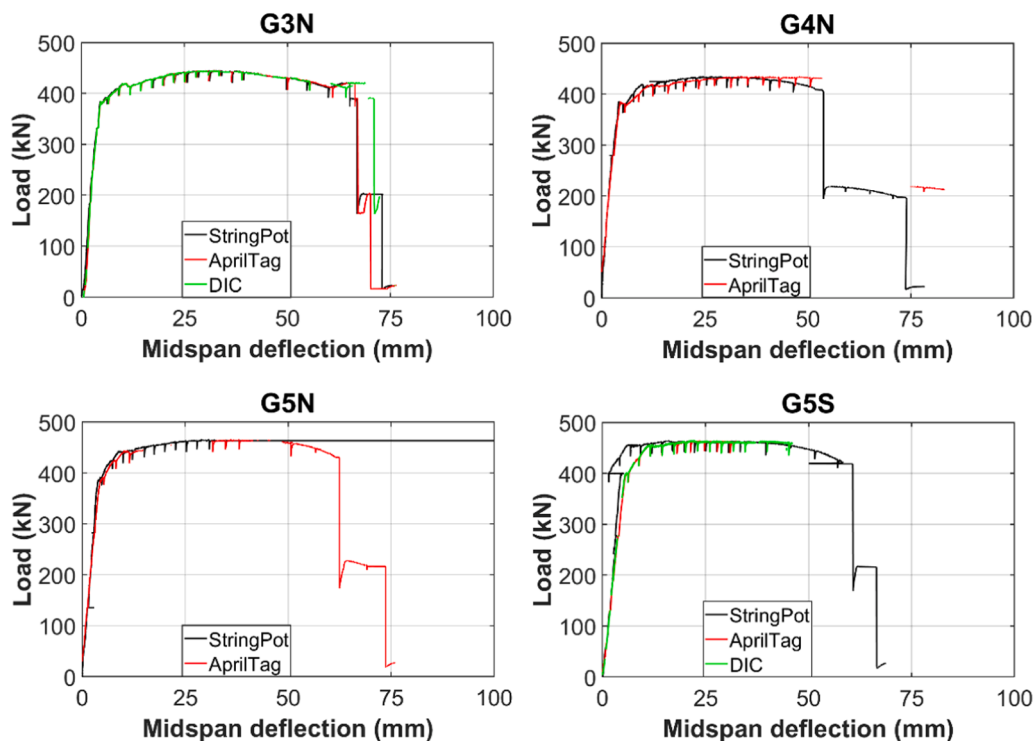


Fig. 7. Girder G3N/G4N/G5N/G5S experimental force versus deflection at the mid-span measured with String Pots (SP), AprilTag, and DIC methods.

measurements from SPs, AprilTag, and/or DIC. Consistent observations with Fig. 6 and Fig. 7 can be made, with nearly identical measurements across modalities. The detachment of the spring pot brackets is clearly seen for girders G2N and G5N at time 5900 s (Fig. 8c) and 3400 s (Fig. 9d), respectively. The sudden erroneous offset of the string pot deflection for G5S is seen at between times 800–1500 s. Shortly

thereafter, the SP measurement followed the AprilTag and DIC measurements with the residual offset (parallel plots > 1500 s).

Lastly, it is seen that for G4N the AprilTag deflection measurement was drifting away from the SP one starting at time 1500 s. To rule out issues with the AprilTag computer vision processing, in Fig. 10 the deflection at the location of the string pot 304.8 mm away from the

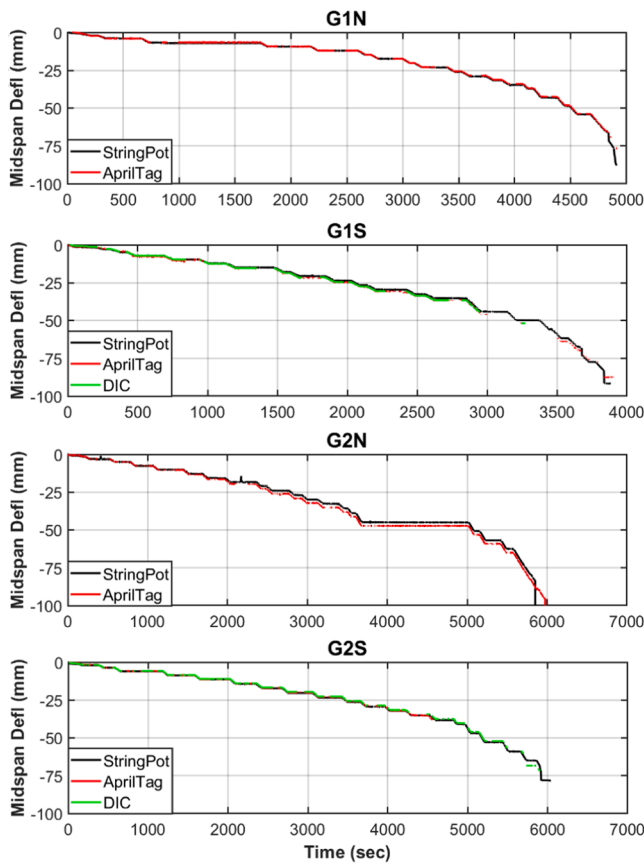


Fig. 8. Time histories of girder G1N/G1S/G2N/G2S experimental mid-span deflection measured with String Pots (SP), AprilTag, and DIC methods.

midspan is plotted against the AprilTag measurement at the same location for G4N. From Fig. 10 it can be seen that the measurements between the SP and AprilTag are almost identical at the location 304.8 mm away from the midspan. To further identify the source of the AprilTag drifting at the midspan location for G4N, a photo of G4N physical specimen at time 3500 s is shown in Fig. 11. It is clearly seen that the AprilTag drift was due to the cracking pattern that resulted in a whole segment of UHPC (with the attached AprilTag) to be disconnected at the bottom of the section at midspan and moved independently, vertically from the rest of the section.

### 5.3. Cracking patterns and failure mode

Each specimen was visually inspected to identify the UHPC cracking pattern during the loading protocol and ultimate failure mode. For example, the evolutions of the visual UHPC cracking patterns are shown in Fig. 12 for the two specimens (i.e., G1S, G3N) with increasing vertical displacement at the midspan. Initially, flexural cracks along the tension soffit were visible underneath the load points and spreading to both sides (between the AprilTag 18 and 20) with increasing load. Furthermore, some mild diagonal cracks began to form near the mid-height of the section when displacement was around 12.80 mm for G3N and 19.05 mm – 25.4 mm for G1S (on the right side). During the widening of the major vertical cracks with increasing displacement magnitude (from 19.05 mm to 31.75 mm), multiple small flexure cracks occurred and distributed within the range of  $x \in (330.2 \text{ mm}, 812.8 \text{ mm})$ .

At failure, the major crack in specimen G1S bifurcated with one branch propagating upward to the loading point, while in specimen G3N it propagated vertically upward through the location of the metal bracket for SP attachment (at displacement 12.7 mm). From the visual inspection, the failure mode was rupture of the tension rebar. Compared

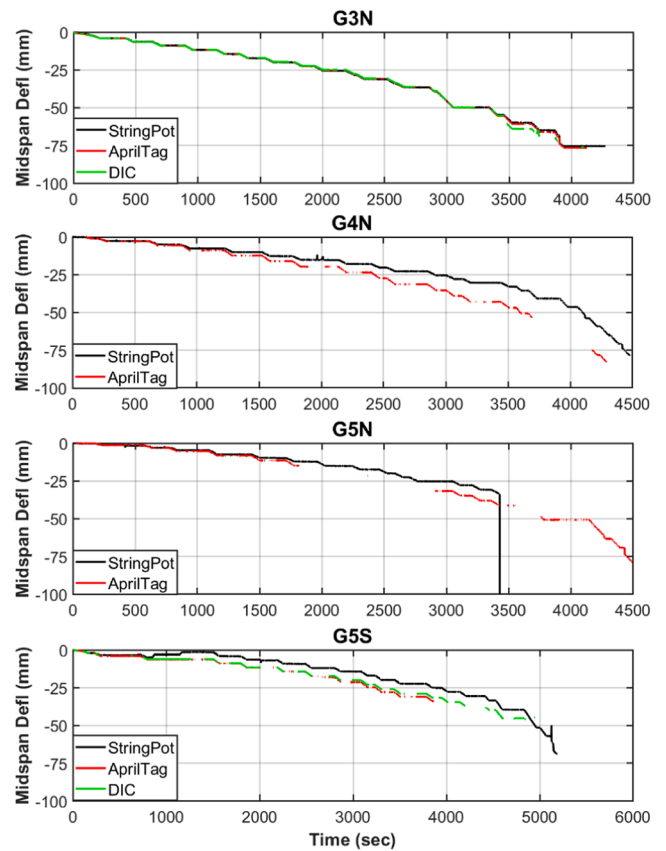


Fig. 9. Time histories of girder G3N/G4N/G5N/G5S experimental mid-span deflection measured with String Pots (SP), AprilTag, and DIC methods.

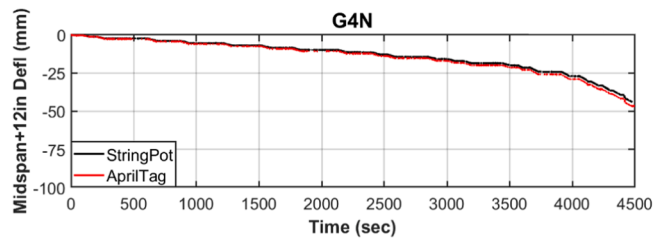


Fig. 10. Time histories of experimental deflection at the location of midspan+304.8 mm on girder G4N measured with String Pots (SP) and AprilTag methods.

to other studies in the literature of similar size UHPC specimens, the force-deformation response of all specimens of the present study exhibited stable capacity and much larger ductility (maximum displacement normalized by yield displacements of approximately 12 to 16 mm). It is hypothesized that some of the ductility contribution comes from the compression steel (as mentioned in the literature review) and large tensile cover; however, it is also hypothesized that local slip occurred on the side of the specimen without the longitudinal hooks that limited the stress transfer to the bar in the constant moment region. The role of bond was explored with the DIC and numerical results below. There was negligible slip measured from the bar protruding outside of the specimen.

### 5.4. DIC strain maps vs FE simulations

The strain distribution maps were studied by comparing the DIC-based strain measurements from the two specimens with the FEA simulated ones. Fig. 13 through Fig. 15 show the comparison between



Fig. 11. Photo of G4N physical specimen at time 3500 s. Partial detachment of UHPC with attached AprilTag (tag-19) at the bottom of the section was observed due to severe cracking.

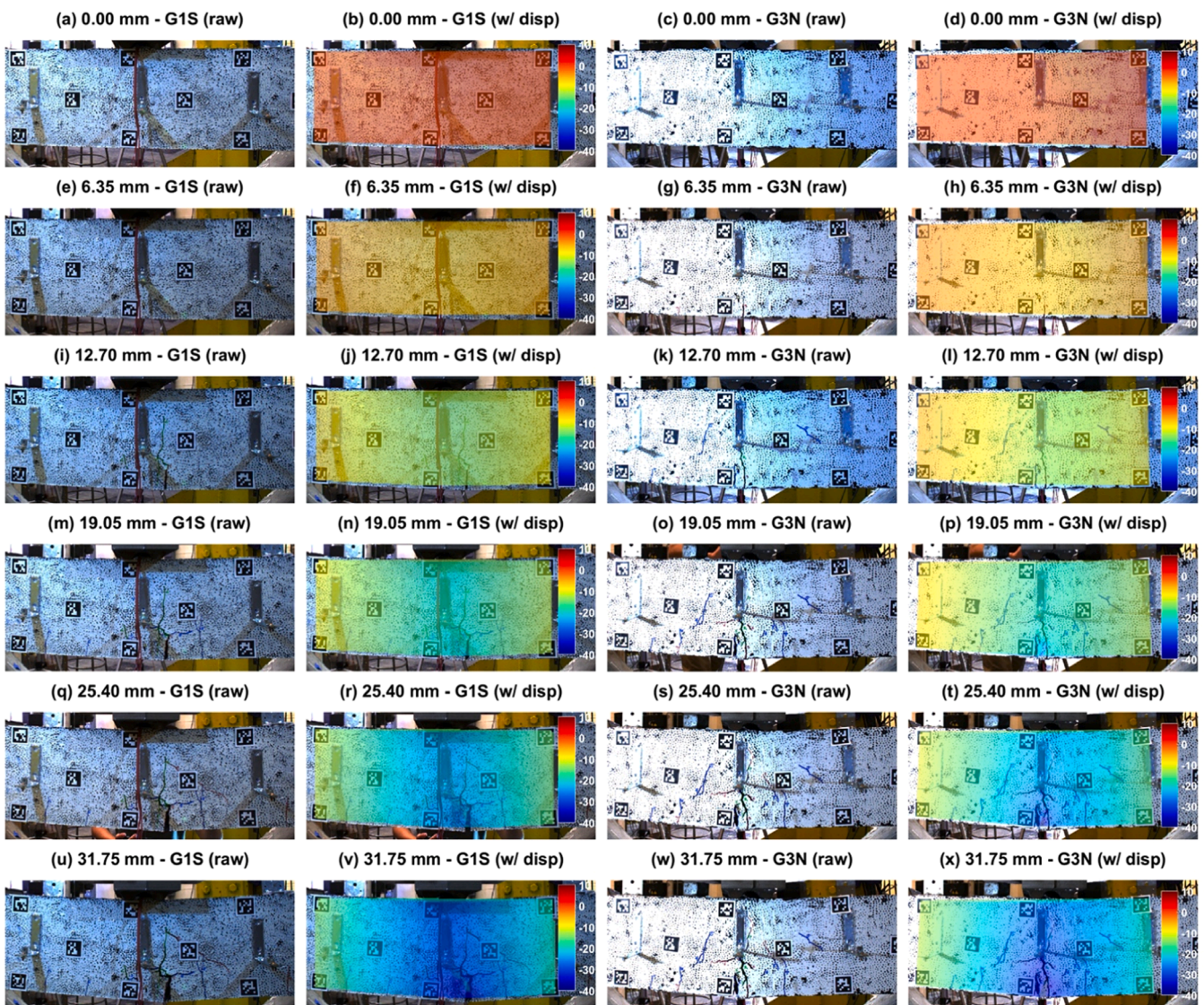


Fig. 12. G1S raw images (1st column) and overlaid vertical displacement distribution (2nd column); G3N raw images (3rd column) and overlaid vertical displacement distribution (4th column).

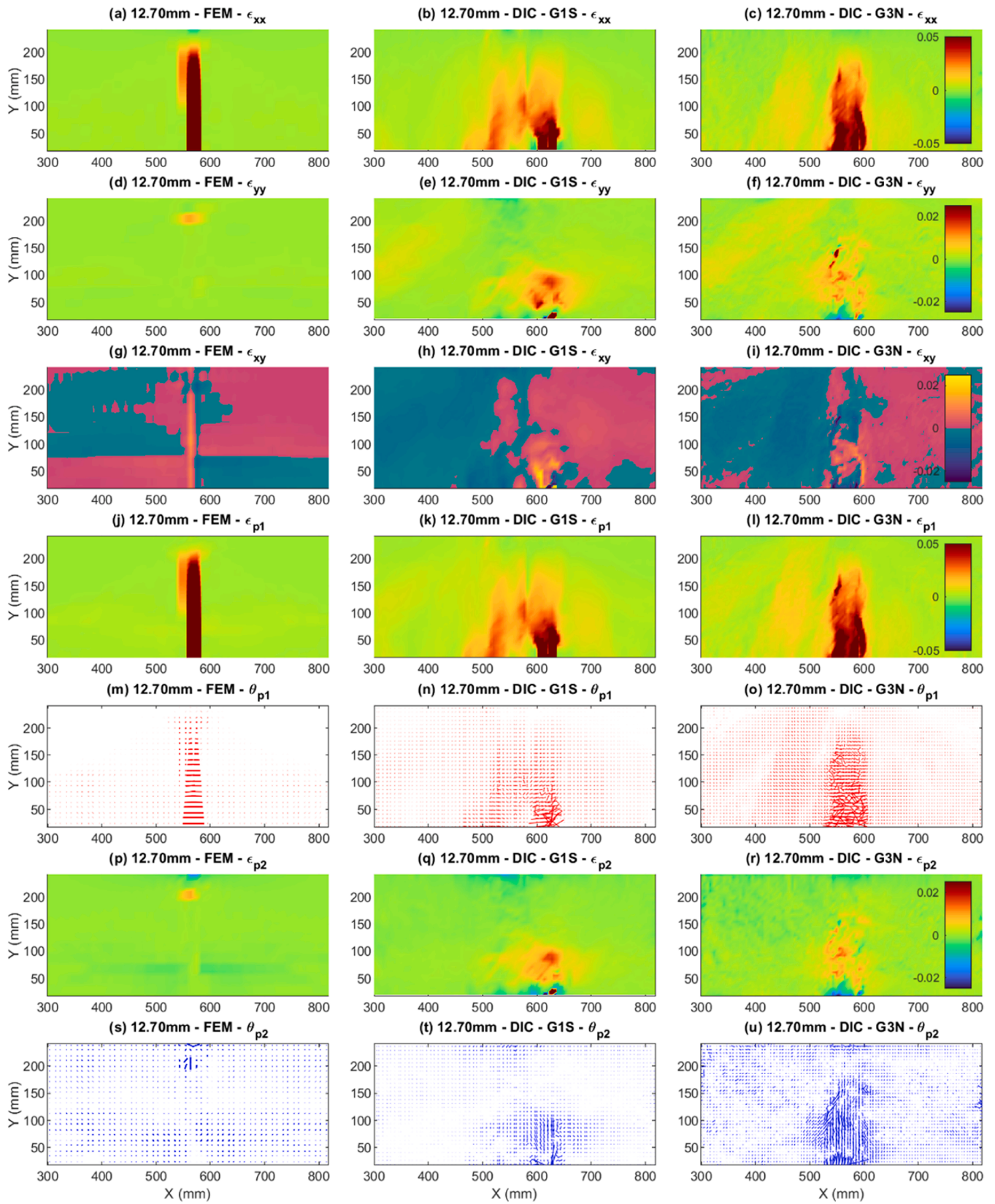


Fig. 13. Comparison of strain distributions ( $\epsilon_{xx}$ ,  $\epsilon_{yy}$ ,  $\epsilon_{xy}$ ,  $\epsilon_{p1}$ ,  $\epsilon_{p2}$ ) and orientations of principal strains ( $\theta_{p1}$ ,  $\theta_{p2}$ ) from FEA simulation (left column), 3D-DIC measurement in specimen G1S (middle column), and 3D-DIC measurement in specimen G3N (right column) when the vertical displacement is 12.70 mm at the midspan.

FE simulation results (as the left column) in the ROI of the girder and the experimental measurements on the specimens G1S (as the middle column) and G3N (as the right column) during three different levels of deflection (12.7 mm, 25.4 mm, and 38.1 mm). All the legend scales for  $\epsilon_{xx}$  and  $\epsilon_{p1}$  are kept as [-5.0 %, +5.0 %] and the legend scales for  $\epsilon_{yy}$ ,  $\epsilon_{xy}$ , and  $\epsilon_{p2}$  are kept as [-2.5 %, +2.5 %] for direct comparison between FE simulations and DIC measurements across the different displacement levels. To illustrate the shear strain patterns (especially the positive and negative signs), two different color bars are used with the top half of viridis (for positive values) and the bottom half of plasma (for positive values), respectively, but the scale is kept same as [-0.25 %, +0.25 %].

At a small displacement level of 12.7 mm, the  $\epsilon_{xx}$  patterns (Fig. 13a-c) expanded with the growing flexure cracks at the bottoms of the girders (Fig. 12). The distribution patterns in  $\epsilon_{xy}$  from DIC (Fig. 13h and Fig. 13i) continued to match well with the one from FEA (Fig. 13g) in space despite the distortions due to the slightly slanted cracks in the actual specimens. On the specimen G1S, one visible crack developed vertically on the right side about 51 mm from the midspan (Fig. 12) which corresponded to both  $\epsilon_{xx}$  (Fig. 13b) and  $\epsilon_{p1}$  (Fig. 13k) at  $Y = \sim 622$  mm. On the specimen G3N, the main crack in the middle continued to develop vertically with an (additional) slanted crack near the middle height of the girder ( $Y = 102$  mm - 152 mm as shown in Fig. 12) which can be inferred from  $\epsilon_{p1}$  (Fig. 13i) and  $\theta_{p1}$  (Fig. 13o). While the FE simulated  $\epsilon_{p1}$  and  $\theta_{p1}$  (Fig. 13j and Fig. 13m) revealed one major vertical crack at 550 mm and 600 mm.

When the displacement level was increased to 25.4 mm (Fig. 14) both experimental  $\epsilon_{xx}$  and  $\epsilon_{p1}$  patterns correspond well with the multiple flexure cracks that gradually developed at the bottoms of the girders (shown visually in Fig. 12). The general distribution patterns in  $\epsilon_{xy}$  from DIC continued to match well with the one from FEA. On both of the specimens, multiple small cracks occurred and distributed within the range of  $x \in [330.2$  mm, 812.8 mm], which corresponded to the  $\epsilon_{p1}$  distributions but with lightly slanted distribution on the sideways away from the center. Inferred from DIC-based  $\theta_{p1}$  orientation distributions, one can distinguish the major cracks (in the centers) with propagation directions perpendicular to the  $\theta_{p1}$  orientations.

When the displacement level was increased to 38.1 mm (Fig. 15), the major flexural cracks at the centers below the loading points continue to widen considerably with the crack width of 3 mm – 4 mm. The major crack in specimen G1S propagated in multiple directions from other cracks forming tree branch-like crack networks which can be inferred by the experimental  $\theta_{p1}$  distributions (Fig. 15n). Of particular note is the ability of the high-resolution computer vision system to measure cracking strains that are difficult to discern from the visual observations (Fig. 15n and Fig. 15o).

The planar FEA model adopted a fixed crack orientation model with no self-weight. The fixed crack orientation assumption in the simulation caused a concentration of the principal cracking strain between the load points at the bottom soffit and a vertical crack. The continuum model was smeared and therefore exhibited no heterogeneous features of UHPC material and the underlying rebar, which would alter the orientation or propagation of the first crack (note G3N is more like the FEA results than G1S in Figs. 13–15). The asymmetry in vertical crack location was properly captured when comparing DIC and FEA due to the structural design where the longitudinal rebar was not hooked on the right side. The crack distribution and strain distribution also depend on the (local) fiber orientation and fiber spatial distributions, whereas in reality a specimen exhibits preferred alignment at the from boundaries due to the flow front and the distribution that varies spatially. Improving the qualitative agreement between model and experiment may be achieved with a rotating crack model or stochastic crack orientation and propagation based on linear or nonlinear fracture mechanics or other discrete or extended finite element methods.

## 5.5. Sectional analysis

The predicted load-displacement curves obtained using both the sectional analysis (with one-dimensional elements), the plane stress model, and two of the experimental results (G1N, G1S) are presented together in Fig. 16. The overestimates in the load predicted using the one-dimensional model are consistent with the moment-curvature analysis sectional results described previously. The overestimate of the nominal and ultimate capacities is due to several factors (as with any comparison between theory and experiment); however, the primary reason is the lack of the interfacial behaviors in the section model. Yoo and Yoon [45] and Zhang et al. [47] also observed this overprediction, and both had straight longitudinal tension bars without hooks. The stress-slip compliance in the plane stress model (that better reproduces the ductility observed in the experiment) prevents the rebar stress from increasing rapidly above yield. The steel rebar stress softens rapidly after reaching the ultimate stress, which manifests as the sudden decrease in the 1D force-displacement curve that occurs at a much smaller displacement (than planar model and experiment) due to the plane sections assumption.

## 6. Conclusions

The experimental program of eight large-scale flexural specimens investigated the behavior of monolithic UHPC girders using both physical and vision-based measurement systems. The girders were tested monotonically to failure using a four-point bending setup. Statistically, there was consistency in all eight experimental test results in terms of stiffness, strength, and ultimate displacements. The application of a fused measurement system provided redundancy in measurements and complemented the advantages of each method. For example, the point-wise photogrammetric (AprilTag) measurements and physical (string pot) measurements enriched the understanding in the structural behavior of global displaced shape and the local rigid body movement around the visible surface cracks. Both AprilTag and 3D-DIC methods yielded the same point-wise displacement measurements. The multi-camera system provided the noncontact setup that was shared between AprilTag and 3D-DIC measurements and allowed more versatile deployments of cameras near specimens.

The FEA and 3D-DIC full-field measurements used were calibrated independently. The FEA included an explicit bond-slip model to simulate the interface between the rebars and UHPC. The bond model parameters used in the FEA were calibrated from a previous study of small flexural UHPC specimens [16]. From the FEA results, a region of slipping was observed for large deflections spreading from the midspan towards the straight bar end (not hooked on the right side of girders, as shown in Fig. 1), preventing an increase of rebar stress to ultimate as indicated by sectional analysis results (or continuum analysis with a higher bond strength). The large ductility at constant load levels (friction-like behavior) in the experiments appeared to be due to this free bar boundary condition and slip. The comparison between FEA and 3D-DIC strain map, deflection, and cracking results showed consistent principal strain magnitude/direction and crack propagation trends.

The shear span-to-depth ratio of the UHPC girders tested was 2, with stable peak strength and flexural cracks including a single large crack opening underneath the load point area, consistent with other studies with similar aspect ratios. However, while in other studies the peak strength was followed by post-peak softening, in the present study the UHPC specimens exhibited a stable capacity plateau to larger ductility values. Ultimately, the failure mode was rupture of the tension rebar, however at much larger deflections due to the limited increase of stresses above yield as a result of the slip of the bars. The consequence was larger deflection/ductility values observed using the fused measurement system, extending the current knowledge of flexural behavior of large monolithic UHPC components.

The results from the present study showed that large monolithic

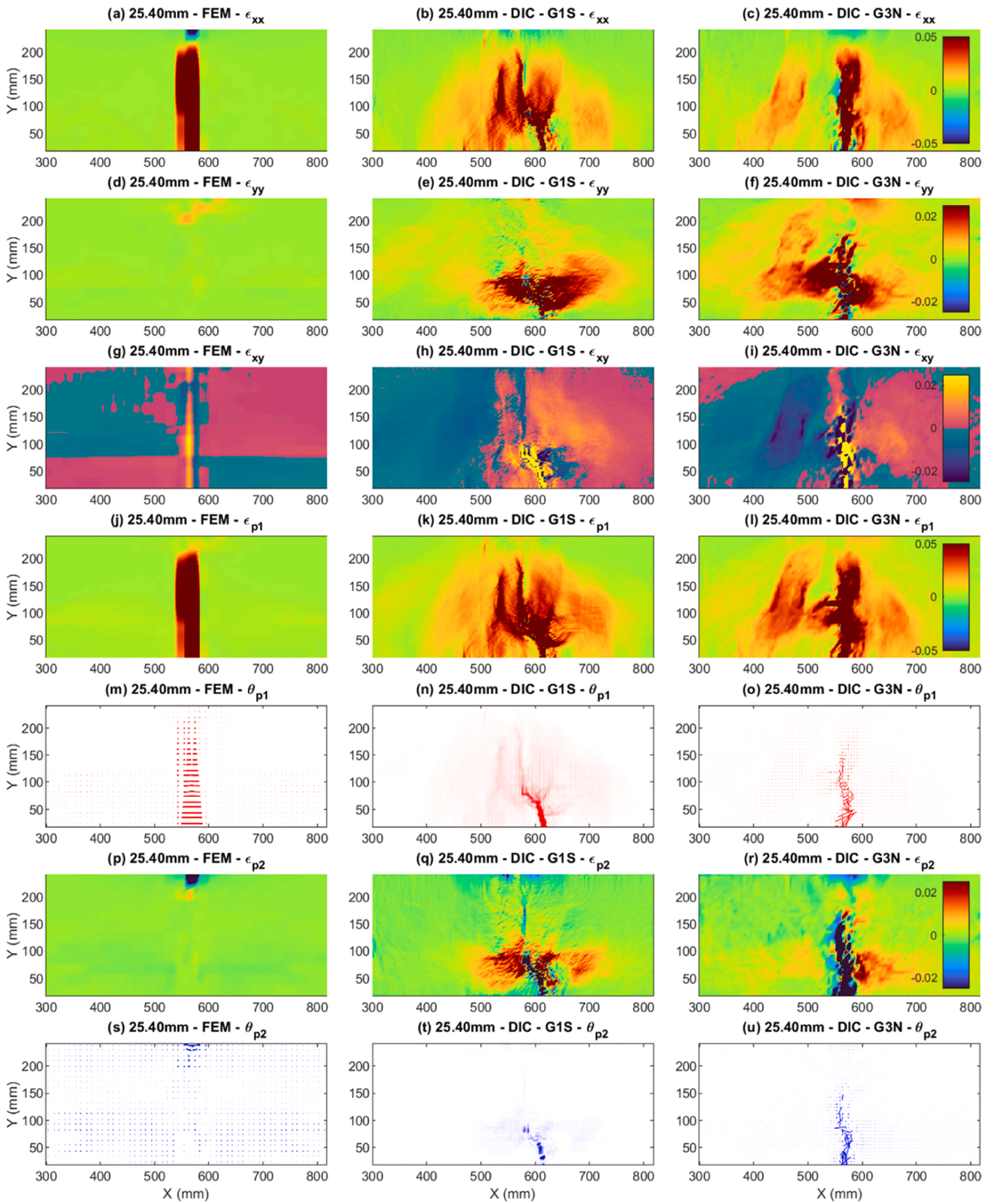


Fig. 14. Comparison of strain distributions ( $\epsilon_{11}$ ,  $\epsilon_{22}$ ,  $\epsilon_{12}$ ,  $\epsilon_{p1}$ ,  $\epsilon_{p2}$ ) and orientations of principal strains ( $\theta_{p1}$ ,  $\theta_{p2}$ ) from FEA simulation (left column), 3D-DIC measurement in specimen G1S (middle column), and 3D-DIC measurement in specimen G3N (right column) when the vertical displacement is 25.40 mm at the midspan.

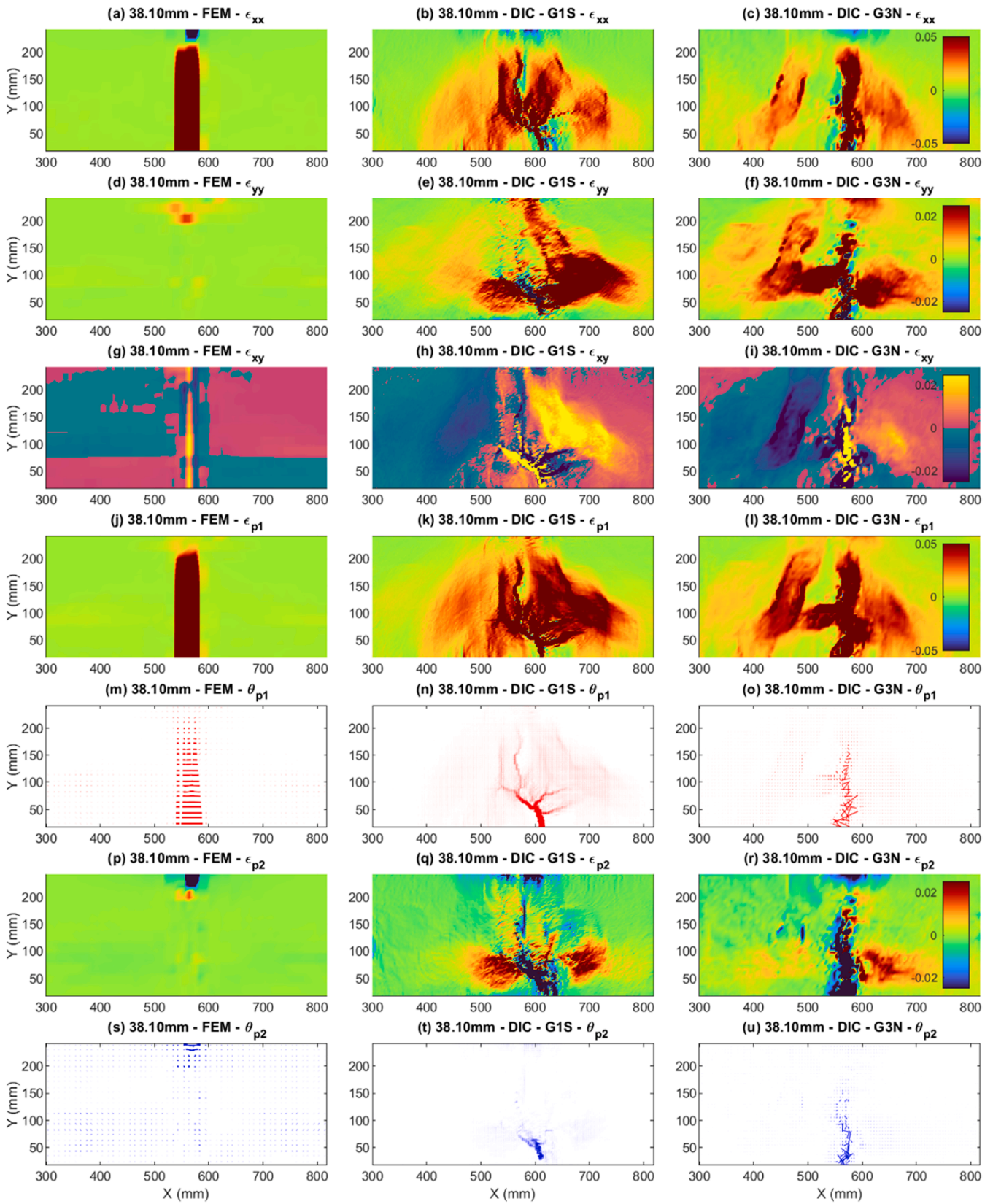
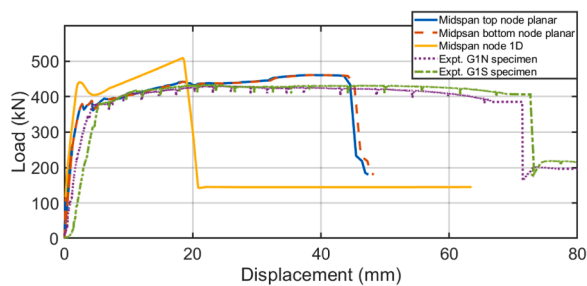


Fig. 15. Comparison of strain distributions ( $\epsilon_{11}$ ,  $\epsilon_{22}$ ,  $\epsilon_{12}$ ,  $\epsilon_{p1}$ ,  $\epsilon_{p2}$ ) and orientations of principal strains ( $\theta_{p1}$ ,  $\theta_{p2}$ ) from FEA simulation (left column), 3D-DIC measurement in specimen G1S (middle column), and 3D-DIC measurement in specimen G3N (right column) when the vertical displacement is 38.10 mm at the midspan.



**Fig. 16.** Comparison of one-dimensional model, plane stress model, and experimental (G1S, G1N) load-displacement results.

UHPC flexural specimens have excellent performance with stable flexural cracking patterns that did not transition to flexural-shear or shear failure even for large deflection/ductility values. Not only did the fused computer vision results render traditional physical measurements redundant, but also can generate full-field displacement and strains on full-scale/near full-scale UHPC. Comparison of full-field measurements with FE analysis results extends knowledge and capabilities beyond single-point measurements for future numerical studies. Future work will be to extend the measurement systems to testing large-scale UHPC long-span flexural girders and beam-column connections that include cyclic loading and study of the rebar slipping phenomenon in UHPC under reversed loading.

#### CRediT authorship contribution statement

**G. Apostolakis:** Conceptualization, Methodology, Investigation, Writing, Supervision. **K. R. Mackie:** Conceptualization, Methodology, Investigation, Writing, Supervision. **M. Iraniparast:** Visualization, Investigation, Software, Validation. **P. Sun:** Conceptualization, Methodology, Investigation, Software, Validation, Writing, Supervision.

#### Declaration of Competing Interest

The authors declare that they have no known competing financial interests or personal relationships that could have appeared to influence the work reported in this paper.

#### Acknowledgements

The authors thank Dr. Miles Zeman (Dura-Stress Inc) and Cor-Tuf UHPC for providing the Cor-Tuf CT25 UHPC material used in the experimental study. The authors also thank graduate research assistants Mr. Tiancheng Wang and Mr. Mohammad Vasef, and undergraduate research assistant Ms. Lisa Barra for helping prepare and conduct the experiments.

#### References

- Ahmad S, Bahij S, Al-Osta MA, Adekunle SK, Al-Dulajjan SU. Shear behavior of ultra-high-performance concrete beams reinforced with high-strength steel bars. *Acids Struct J* 2019;V. 116(4).
- Bermudo Gamboa C, Martín-Béjar S, Trujillo Vilches FJ, Castillo López G, Sevilla Hurtado L. 2D–3D digital image correlation comparative analysis for indentation process. *Materials* 2019;12(24):4156.
- Blaber J, Adair B, Antoniou A. Ncorr: open-source 2D digital image correlation matlab software. *Exp Mech* 2015;55(6):1105–22.
- Chu TC, Ranson WF, Sutton MA. Applications of digital-image-correlation techniques to experimental mechanics. *Exp Mech* 1985;25:232–44.
- Corr D, Accardi M, Graham-Brady L, Shah S. Digital image correlation analysis of interfacial debonding properties and fracture behavior in concrete. *Eng Fract Mech* 2007;74(1–2):109–21.
- Dadmand B, Sadaghian H, Khalilzadehtabrizi S, Pourbaba M, Shirdeh M, Mirmiran A. Studying the compressive, tensile and flexural properties of binary and ternary fiber-reinforced UHPC using experimental, numerical and multi-target digital image correlation methods. *Case Stud Constr Mater* 2023;18:e01865.
- Destrebecq JF, Toussaint E, Ferrier EJEM. Analysis of cracks and deformations in a full scale reinforced concrete beam using a digital image correlation technique. *Exp Mech* 2011;51:879–90.
- Dong CZ, Catbas FN. A review of computer vision-based structural health monitoring at local and global levels. *Struct Health Monit* 2021;20(2):692–743.
- Eligehausen R, Popov EP, Bértero VV. Local bond stress-slip relationships of deformed bars under generalized excitations: experimental results and analytical model. Earthquake Engineering Research Center. Berkeley: University of California; 1983.
- Feng Z, Li C, Yoo D-Y, Pan R, He J, Ke L. Flexural and cracking behaviors of reinforced UHPC beams with various reinforcement ratios and fiber contents. *Eng Struct* 2021;248:113266.
- Feng J, Shao X, Qiu M, Li H, Gao X, Huang Z. Reliability evaluation of flexural capacity design provision for UHPC beams reinforced with steel rebars/prestressing tendons. *Eng Struct* 2024;300:117160.
- FHWA (2018). Properties and Behavior of UHPC-Class Materials (FHWA-HRT-18-036). *Federal Highway Administration*, McLean, VA.
- FHWA (2023). Structural Design with Ultra-High Performance Concrete (FHWA-HRT-23-077). *Federal Highway Administration*, McLean VA.
- Ghorbani R, Matta F, Sutton MA. Full-field deformation measurement and crack mapping on confined masonry walls using digital image correlation. *Exp Mech* 2015;55:227–43.
- Harenberg S, Pahn M, Malárics-Pfaff V, Dehn F, Caggiano A, Schicchi DS, et al. Digital image correlation strain measurement of ultra-high-performance concrete-prisms under static and cyclic bending-tensile stress. *Struct Concr* 2019;20(4):1220–30.
- Hock J, Mackie KR, Apostolakis G, Wang T. Flexural non-contact lap splices in ultra-high performance concrete. *ACI Structures*. Journal 2024;121(1).
- Hung CC, El-Tawil S, Chao SH. A review of developments and challenges for UHPC in structural engineering: behavior, analysis, and design. *J Struct Eng* 2021;147(9):03121001.
- Kodsy A, Morcouc G. Shear strength of ultra-high-performance concrete (uhpc) beams without transverse reinforcement: prediction models and test data. *Materials* 2022;15:4794.
- Küntz M, Jolin M, Bastien J, Perez F, Hild F. Digital image correlation analysis of crack behavior in a reinforced concrete beam during a load test. *Can J Civ Eng* 2006;33(11):1418–25.
- Lee J, Lee KC, Lee S, Lee YJ, Sim SH. Long-term displacement measurement of bridges using a LiDAR system. *Struct Control Health Monit* 2019;26(10):e2428.
- Li D, Huang P, Chen Z, Yao G, Guo X, Zheng X, et al. Experimental study on fracture and fatigue crack propagation processes in concrete based on DIC technology. *Eng Fract Mech* 2020;235:107166.
- Meng W, Bachilo SM, Parol J, Nagarajaiah S, Weisman RB. Near-infrared photoluminescence of Portland cement. *Sci Rep* 2022;12(1):1197.
- Meng W, Pal A, Bachilo SM, Weisman RB, Nagarajaiah S. Next-generation 2D optical strain mapping with strain-sensing smart skin compared to digital image correlation. *Sci Rep* 2022;12(1):11226.
- Mobasher B, Li A, Yao Y, Arora A, Neithalath N. Characterization of toughening mechanisms in UHPC through image correlation and inverse analysis of flexural results. *Cem Concr Compos* 2021;122:104157.
- Nadler B, Rubin MB. A new 3-D finite element for nonlinear elasticity using the theory of a Cosserat point. *Int J Solids Struct* 2003;40(17):4585–614.
- Niu Y, Huang H, Wei J, Jiao C, Miao Q. Investigation of fatigue crack propagation behavior in steel fiber-reinforced ultra-high-performance concrete (UHPC) under cyclic flexural loading. *Compos Struct* 2022;282:115126.
- Niu Y, Huang H, Zhang J, Jin W, Wei J, Yu Q. Development of the strain field along the crack in ultra-high-performance fiber-reinforced concrete (UHPFRC) under bending by digital image correlation technique. *Cem Concr Res* 2019;125:105821.
- Orteu JJ. 3-D computer vision in experimental mechanics. *Opt Lasers Eng* 2009;47(3–4):282–91.
- Peng F, Yi W, Fang Z. Design approach for flexural strength of reinforced ultra-high-performance concrete members considering size effect. *Acids Struct J* 2022;V. 119(1).
- Qiu M, Hu Y, Shao X, Zhu Y, Li P, Li X. Experimental investigation on flexural and ductile behaviors of rebar-reinforced ultra-high-performance concrete beams. *Struct Concr* 2022;23:1533–54.
- Raju APA, Lewis A, Derby B, Young RJ, Kinloch IA, Zan R, et al. Wide-area strain sensors based upon graphene-polymer composite coatings probed by Raman spectroscopy. *Adv Funct Mater* 2014;24(19):2865–74.
- Saqif MA, Tai Y-S, El-Tawil S. Experimental and computational evaluation of the ductility of UHPC beams with low steel-reinforcement ratios. *J Struct Eng* 2022;148(7):04022077.
- Shen X, Brühwiler E. Influence of local fiber distribution on tensile behavior of strain hardening UHPFRC using NDT and DIC. *Cem Concr Res* 2020;132:106042.
- Singh M, Sheikh AH, Ali MM, Visintin P, Griffith MC. Experimental and numerical study of the flexural behaviour of ultra-high performance fibre reinforced concrete beams. *Constr Build Mater* 2017;138:12–25.
- Solav D, Silverstein A. Duodic: 3d digital image correlation in Matlab. *J Open Source Softw* 2022;7(74):4279.
- Sun P, Bachilo SM, Lin CW, Nagarajaiah S, Weisman RB. Dual-layer nanotube-based smart skin for enhanced noncontact strain sensing. *Struct Control Health Monit* 2019;26(1):e2279.
- Sun P, M. Bachilo S, Lin CW, Weisman RB, Nagarajaiah S. Noncontact strain mapping using laser-induced fluorescence from nanotube-based smart skin. *J Struct Eng* 2019;145(1):04018238.

- [38] Sun W, Weldon BD, McGinnis MJ, Jiang R. Numerical and digital image correlation study of the flexural behavior of prestressed ultra-high-performance concrete beams made from locally available materials. *PCI J* 2024;69(1).
- [39] Sutton MA, Orteu JJ, Schreier H. Image correlation for shape, motion and deformation measurements: basic concepts, theory and applications. Springer Science & Business Media; 2009.
- [40] Turker K, Hasgul U, Birol T, Yavas A, Yazici H. Hybrid fiber use on flexural behavior of ultra high performance fiber reinforced concrete beams. *Compos Struct* 2019;229:111400.
- [41] Wang F, Kan L, Yu J, Duan XZ. Systematic studies on behaviors of ultra-high performance concrete subject to freezing and thawing cycles combining DIC technology. *Constr Build Mater* 2023;388:131580.
- [42] Wang J, Olson E. AprilTag 2: Efficient and robust fiducial detection (, October). In 2016 IEEE/RSJ International Conference on Intelligent Robots and Systems (IROS). IEEE; 2016. p. 4193–8 (, October).
- [43] Yang IH, Joh C, Kim BS. Structural behavior of ultra high performance concrete beams subjected to bending. *Eng Struct* 2010;32(11):3478–87.
- [44] Yang IH, Park J, Bui TQ, Kim KC, Joh C, Lee H. An experimental study on the ductility and flexural toughness of ultrahigh-performance concrete beams subjected to bending. *Materials* 2020;13(10):2225.
- [45] Yoo DY, Yoon YS. Structural performance of ultra-high-performance concrete beams with different steel fibers. *Eng Struct* 2015;102:409–23.
- [46] Zhang Z, Feng Q, Gao Z, Kuang C, Fei C, Li Z, et al. A new laser displacement sensor based on triangulation for gauge real-time measurement. *Opt Laser Technol* 2008; 40(2):252–5.
- [47] Zhang Y, Zhu Y, Qiu J, Hou C, Huang J. Impact of reinforcing ratio and fiber volume on flexural hardening behavior of steel reinforced UHPC beams. *Eng Struct* 2023;285:116067.
- [48] Zou Y. Evaluation of the strain response of FRP partially confined concrete using FEM and DIC testing. *Int J Struct Integr* 2024.